Revision 4

Valleyite: A new magnetic mineral with the sodalite-type structure

Huifang Xu [a*], Seungyeol Lee [a], Hongwu Xu [b], Ryan Jacobs [c], and Dane Morgan [c]

[a] NASA Astrobiology Institute, Department of Geoscience, University of Wisconsin–Madison, Madison, Wisconsin 53706, USA

[b] Earth and Environmental Sciences Division, Los Alamos National Laboratory, Los Alamos, NM 87545, USA

[c] Department of Materials Science and Engineering, University of Wisconsin-Madison, Madison, Wisconsin 53706, USA

*Corresponding author:
Prof. Huifang Xu
Department of Geoscience
University of Wisconsin-Madison
1215 West Dayton Street, A352 Weeks Hall
Madison, Wisconsin 53706
Tel: 1-608-265-5887
Fax: 1-608-262-0693
Email: hfxu@geology.wisc.edu

ABSTRACT

Valleyite, $Ca_4(Fe,Al)_6O_{13}$, is a new sodalite-type mineral discovered in late Pleistocene basaltic scoria from the Menan Volcanic Complex near Rexburg, Idaho, USA. It is an oxidation product of basaltic glass during the early stage of the scoria formation and is associated with hematite (α-Fe_2O_3), maghemite (γ-Fe_2O_3), luogufengite (ε-Fe_2O_3) and quartz on the surface of vesicles. The measured crystal size of valleyite ranges from ~250 nm to ~500 nm. The empirical chemical formula of valleyite is $(Ca_{3.61}Mg_{0.39})(Fe_{3.97}Al_{1.91}Ti_{0.09})O_{13}$. The mineral has a space group of $I\bar{4}3m$; its unit-cell parameter refined from synchrotron X-ray powder diffraction data is: $a = 8.8852(7)$, unit cell volume = 701.46 (17) Å^3, and Z = 2. The seven strongest lines of the obtained X-ray diffraction pattern [d(Å)(I)(hkl)] are: 6.287(43.1)(011); 4.4395(5.3)(002); 3.6284(100)(112); 3.1395(5.2)(022); 2.8011(36.5)(013); 2.5644(29.4)(222); and 2.3750(31.5) (123). The (Fe,Al)-O bond distance and unit cell edge are slightly larger than those reported for synthetic $Ca_4Al_6O_{13}$, presumably due to the presence of the larger Fe^{3+} cations, compared with Al^{3+}, in the structure. Density functional theory calculations predict that valleyite may be a metastable phase at low temperatures. Measured Curie temperatures for valleyite and luogufengite are 645K and 519K, respectively. Their magnetization hysteresis loop indicates the magnetic exchange coupling between valleyite (soft magnet) and luogufengite (hard magnet), which aids in the understanding of magnetic properties and paleo-magnetism of basaltic rocks. This new mineral, valleyite, with the sodalite-type cage structure is potentially a functional magnetic material.

Keywords: Valleyite, Sodalite-type structure, Luogufengite, Hematite, Scoria, Magnetic property, synchrotron X-ray diffraction, Transmission electron microscopy

INTRODUCTION

The new nano-mineral, valleyite, was discovered in late Pleistocene (~10,000 years) basaltic scoria from the Menan Volcanic Complex near Rexburg, Idaho, USA. The Menan Volcanic Complex consists of broad, flat volcanoes, formed by low-viscosity eruptions, with tholeiitic basalts dominating the surface exposures (Russell and Brisbin, 1990; Hackett and Morgan, 1988; Hughes et al. 1999). The formation of scoria was related to the interaction of external water with the late-stage (late Pleistocene) eruption in the center of the Menan complex (Hackett and Morgan, 1988; Hughes et al. 1999). In general, the scoria with a brown and dark color contains more valleyite nano-grains than the red scoria.

In this study, the crystal structure, chemical composition, and magnetic properties of valleyite are presented. The mineral name has been approved by the Commission on New Minerals, Nomenclature and Classification (CNMNC) of the International Mineralogical Association, (IMA 2017-026) (Xu et al. 2017a). The newly discovered mineral species of $Ca_4(Fe,Al)_6O_{13}$ is named after Prof. John W. Valley (born in 1948) of the University of Wisconsin – Madison. Prof. Valley was the President of the Mineralogical Society of America (MSA) during 2005-2006. His groundbreaking contributions to mineralogy, petrology, and geochemistry have led to a deeper understanding of Earth's crustal evolution from early Earth to the Anthropocene. Valleyite is deposited in the collection of the Geology Museum of the Department of Geoscience, University of Wisconsin-Madison, with specimen numbers UWGM 2352 and UWGM2353.

SAMPLES AND METHODS

The samples were carefully scratched off from the vesicles' surfaces of the collected basaltic scoria (Supplementary Fig. S1). These samples were placed in a 10M NaOH solution at 80 °C for 2 days to remove the silicate glass by following previous procedures (Xu et al. 2017b; Lee et al. 2018). After washing the sample powders with distilled water several times, valleyite was enriched using a magnetic bar to reduce the portion of non-magnetic minerals. The valleyite sample was further enriched by an iron needle to pick up the remnant magnetized crystals. These magnetic enrichment steps were repeated 5-7 times.

For comparison, a synthetic valleyite sample was prepared through thermal decomposition of a clay mineral, nontronite, from Quincy, WA, as described in Lee and Xu (2016). Crushed nontronite powders were loaded into an alumina boat, which was then placed in a furnace to be heated at 850 °C for 2 days in air. After heating, the sample was quenched in cold water. Isolation of the ferric oxides from amorphous SiO_2 was performed by dissolving the sample in a 10 M NaOH solution at 80 °C for 2 days. After washing with distilled water several times, synthetic valleyite, together with luogufengite and hematite, was obtained. The synthetic valleyite can also be enriched using the magnetic enrichment steps for natural valleyite, described above.

High-resolution X-ray powder diffraction data were collected at beamline 11-BM of the Advanced Photon Source (APS) at Argonne National Laboratory. Diffraction patterns were recorded using a wavelength (λ) of 0.414631 Å for the natural sample and of 0.414584 Å for the synthetic sample. Finely ground powders of the samples were placed into polyimide tubes with an inner diameter of 1 mm for the synchrotron XRD measurements. The sample-to-detector distance and beam center position were calibrated using a LaB_6 standard. Diffraction data of an empty polyimide tube were collected for background removal in the data reduction. The crystal structure of valleyite and the ratios of mineral phases presented in the sample were determined with the Rietveld method using the MDI JADE 9 software. A pseudo-Voigt function was used to fit the peak profiles, accounting for the effects of nano-grain broadening and lattice strains. Positions for the Fe and one oxygen atom (O2) in valleyite are at special positions. Because the sample contains only ~10 wt.% of valleyite, it is not possible to accurately refine the U_{iso} values. Thus we fixed the U_{iso} values at those for the synthetic $Ca_4Al_6O_{13}$ phase reported by Peters et al. (2007).

Bright-field and dark-field transmission electron microscopy (TEM) images, high-resolution TEM (HRTEM) images, and selected-area electron diffraction (SAED) patterns were obtained using a Philips CM200-UT microscope operated at 200 kV. TEM samples were prepared by depositing a suspension of the enriched samples on a lacy carbon-coated Cu grid. The chemical composition was obtained using a TEM-EDS system equipped with a Li-drifted Si detector (Oxford instruments Link ISIS). An electron beam diameter of ~50 nm was used for collecting X-ray EDS spectra with fayalite, anorthite, forsterite, and titanite as the standards to quantify the element fractions of Fe, Ca, Al, Mg, and Ti in the samples.

Magnetic hysteresis loops of the powder samples were obtained using a superconducting quantum interference device (SQUID) magnetometer (MPMS 3, Quantum Design). The measurements were conducted under applied magnetic fields of -1 to 1 Tesla at room temperature. From 300K to 1000 K, the thermal evolution of magnetization has been measured under an applied 1 kOe in a Lakeshore Vibrating Sample Magnetometer (VSM).

To study the stability of valleyite, we conducted theoretical calculations using density functional theory (DFT) as implemented in the Vienna Ab Initio Simulation Package (VASP) (Kresse and Furthmüller, 1996). An end-member valleyite $Ca_4Fe_6O_{13}$ supercell containing two formula units (46 atoms) and multiple valleyite $(Ca_{3.5}Mg_{0.5})(Fe_4Al_{2-x}Ti_x)O_{13}$ (x = 0, 0.125, 0.5) supercells containing two formula units (46 atoms, $x = 0$ and 0.5) and 16 formula units (368 atoms, $x = 0.125$) were simulated in the sodalite-type structure (space group $I\bar{4}3m$). We used projector augmented wave (PAW)-type (Kresse and Joubert, 1999) pseudopotentials fit for the Perdew-Burke-Ernzerhof (PBE) (Perdew et al. 1996) generalized gradient approximation (GGA) exchange-correlation functional. We used the PBE GGA exchange-correlation functional with Hubbard U correction (GGA+U) (Anisimov et al. 1997) with $U = 5.3$ eV for the Fe atoms, consistent with the value used in the Materials Project database (Jain et al. 2013). A planewave energy cutoff of 500 eV was used and all calculations were performed with spin polarization enabled. Both ferromagnetic and antiferromagnetic spin configurations were simulated. For the antiferromagnetic configuration, the magnetic moments were ordered to contain an equal number of up and down spins on Fe-containing {100} planes. For the case of $(Ca_{3.5}Mg_{0.5})(Fe_4Al_{2-x}Ti_x)O_{13}$ ($x = 0$), four different antiferromagnetic spin orderings were considered to test the effect of spin ordering on the total energy. The energy variation with different antiferromagnetic orderings was found to be ~20 meV/Fe, which is small and on the order of kT at room temperature. For the composition of $(Ca_{3.5}Mg_{0.5})(Fe_4Al_{2-x}Ti_x)O_{13}$ ($x = 0$), 4 different Mg configurations on the (Ca, Mg) sublattice and 5 different Al configurations on the (Fe, Al) sublattice were performed, and for the composition $(Ca_{3.5}Mg_{0.5})(Fe_4Al_{2-x}Ti_x)O_{13}$ ($x = 0.5$), 4 different Ti configurations on the (Al, Ti) sublattice were performed in order to assess the impact of the configuration of minor alloying cations on the calculated stability. Overall, it was found that the impact of alloying element configuration on the total energy is small, on the order of ~50 meV/Mg, ~35 meV/Al and ~100 meV/Ti for Mg, Al and Ti alloying, respectively. These total energy differences arising from different alloying cation configurations resulted in very small differences in calculated stability and formation energies, typically < 5 meV/atom. Brillouin zone sampling was performed with the Monkhorst-Pack scheme with a 4×4×4 *k*-point mesh (46 atom supercells) and 2×2×2 *k*-point mesh (368 atom supercell) (Monkhorst and Pack, 1976). All key input/output calculation files are included as part of the supplementary materials, including relaxed structures, calculated total energies and magnetic moments.

Stability calculations were performed using convex hull analysis of the DFT-calculated total energies as implemented in the Pymatgen (Ong et al. 2013) toolkit assuming a system open to oxygen and ambient conditions of $T = 298$ K and $p(O_2) = 0.2$ atm following previous work (Jacobs et al. 2018). These conditions result in an oxygen chemical potential of $\mu_O = -5.25$ eV/O, which was calculated using experimental thermochemical data and standard DFT thermochemistry equations following previous work (Jacobs et al. 2012). In addition to convex hull analysis as a probe of the material stability, we also calculated the formation energy of valleyite relative to decomposition to its constituent binary oxides of the same oxidation states. For example, for the case of $(Ca_{3.5}Mg_{0.5})(Fe_4Al_{2-x}Ti_x)O_{13}$ ($x = 0.5$), the reaction formation energy of $3.5CaO + 0.5MgO + 2Fe_2O_3 + 0.75Al_2O_3 + 0.5TiO_2 \rightarrow (Ca_{3.5}Mg_{0.5})(Fe_4Al_{1.5}Ti_{0.5})O_{13} + 0.125O_2$ was calculated using DFT-calculated binary oxide energies tabulated in the Materials Project database. Note that these oxide reference states are all modelled as ferromagnetic. The formation energies are included as a second stability metric in addition to convex hull analysis based on recent work (Ye et al. 2018) claiming that convex hull analysis can yield results that vary unpredictably even for similar materials chemistries.

RESULTS AND DISCUSSION

The synchrotron XRD pattern of a treated scoria sample reveals the occurrence of valleyite, together with luogufengite, hematite, calcite, and quartz (Fig. 1). Major peaks from valleyite that occur at the low-angle side can be clearly resolved (Fig. 1). Table 1 lists the diffraction peaks of valleyite. The diffraction peaks from valleyite are sharper than those from nanophase luogufengite, which has a smaller average size (40 nm).

The nano-crystals of valleyite were characterized using HRTEM and SAED (Figs. 2 and 3). The size of valleyite crystals ranges from ~250 nm to ~500 nm. SAED patterns indicate that valleyite has cubic ($I\bar{4}3m$) symmetry. The mineral displays crystallographic forms of {100}, {111}, and $\{1\bar{1}1\}$ (Figs. 2, 3). Its morphology is illustrated in supplementary materials (Figure S2). The chemical formula, $(Ca_{3.61}Mg_{0.39})(Fe_{3.97}Al_{1.91}Ti_{0.09})O_{13,}$ was calculated from X-ray EDS spectra (Table 2). A representative X-ray EDS spectrum from valleyite is illustrated in figure 3e.

The crystal structure was determined based on an input model of synthetic sodalite-like phase $Ca_4Al_6O_{13}$ (Peters et al. 2007) with our EDS-measured formula (Table 2) using Rietveld analysis. Fractional coordinates, occupancies and isotropic displacement parameters of all the atoms are listed in Table 3. The structure of valleyite consists of a framework of corner-sharing $(Fe,Al)O_4$ tetrahedra with Ca^{2+} cations occupying the cavities (Fig. 4). Comparisons among sodalite (Hassan et al., 2004), synthetic $Ca_4Al_6O_{13}$ (Peters et al., 2007), and valleyite are illustrated in Figure 5. The structures with different sizes of tetrahedra display a different degree of distortion in their di-trigonal rings (Fig. 5). The (Fe,Al)-O bond distance and unit cell edge are slightly larger than those reported for synthetic $Ca_4Al_6O_{13}$ due to the presence of the larger Fe^{3+} cations, compared with Al^{3+}, in the structure (Table. 4).

The synthetic valleyite, together with ε-Fe_2O_3 (synthetic luogufengite) and α-Fe_2O_3 (synthetic hematite), were obtained from thermal decomposition of a Fe(III)-dominated clay mineral of nontronite (see Figure S3 in supplementary materials). The synthetic phases have approximately the same particle sizes as their natural phase counterparts, based on the similar

FWHMs (Full Width at Half Maximum) of their XRD peaks.

Valleyite is a magnetic material because it can be readily picked up and enriched together with luogufengite from pre-magnetized powders using an iron needle. Figure 6 shows evolution of magnetization of the treated sample from 300 to 1000 K, indicating Curie temperatures for luogufengite and valleyite are 519K and 645K and, respectively. The Curie temperature for luogufengite is very close to a reported value of a synthetic Al-bearing ε–Fe_2O_3 (Nanai et al., 2009). The magnetization of valleyite is estimated to be ~9.2 emu/g at room temperature based on the ~0.9 emu/g demagnetization of 9.8(3) wt. % valleyite in the analysed sample. The magnetic transitions are relatively wide, which can be attributed to the large particle size distribution (Tucek et al. 2010). The remaining magnetic signal above 645 K is associated with canted antiferromagnetic hematite (López-Sánchez et al. 2016).

The magnetic hysteresis loop of the treated sample (a mixture of luogufengite, hematite, and valleyite with a small amount of calcite and quartz; Figure 1) shows a coercive field of 0.17 Tesla (T) with a remnant magnetism of ~9.5 emu g^{-1} at room temperature (Figure 7). The shape of the hysteresis loop is typical of an exchange coupled phase of magnetically hard and soft magnets, indicating the magnetic exchange coupling between luogufengite (hard magnet) and valleyite (relatively soft magnet) (Neupane et al. 2017). Figure 6a shows a magnetic hysteresis loop of synthetic Al-bearing luogufengite with ~ 10 mole % of Al in the structure (Ohkoshi et al. 2005). The small amount of hematite cannot affect the hysteresis loop due to its weak magnetic property (Supplementary Figure S4) (Ohkoshi et al. 2005). The hysteresis loop of valleyite is similar to a soft magnet in the magnetic coupling system of $SrFe_{12-y}Al_yO_{19}$ (soft magnet) / $Ni_{0.5}Zn_{0.5}Fe_2O_4$ (hard magnet) (Neupane et al. 2017), and hard-soft magnetic nanocomposite with the composition of (90%) $SrFe_{10}Al_2O_{19}$ / (10%) $Co_{0.8}Ni_{0.2}Fe_2O_4$ (Torkian and Ghasemi, 2018).

Strong exchange coupling occurs between a soft magnet and hard magnet in a magnetic nanocomposite when the radius of the soft magnet is smaller than the critical exchange length for the soft magnet (Kneller and Hawig, 1991). The critical exchange length for magnetite ranges from ~ 50 nm to 1000 nm (Muxworthy and Williams, 2006). The observed crystal size of valleyite is within this range.

DFT calculations were performed on a synthetic ($Ca_4Fe_6O_{13}$) and multiple natural ($Ca_{3.5}Mg_{0.5}(Fe_4Al_{2-x}Ti_x)O_{13}$) valleyite compositions, including the case of $x = 0.125$, which has a simulated composition close to the measured valleyite composition of $(Ca_{3.61}Mg_{0.39})(Fe_{3.97}Al_{1.91}Ti_{0.09})O_{13}$ from EDS (see Supplementary Figure 5). The main goal of these DFT calculations is to obtain a qualitative scale of the stability of valleyite. Table 5 contains a summary of the stability calculations for each valleyite composition considered in this work.

From Table 5, the stability calculations of synthetic valleyite $Ca_4Fe_6O_{13}$ indicate that it is 105 (42) meV/atom above the convex hull and 70 (7) meV/atom vs. decomposition to binary oxides for ferromagnetic (antiferromagnetic) configurations, respectively. The substitution of 12.5% of Ca with Mg and 33% of Fe with Al (close to the Mg and Al content in natural valleyite) to make $Ca_{3.5}Mg_{0.5}(Fe_4Al_2)O_{13}$ results in a stability of 86 (74) meV/atom above the convex hull and 41 (29) meV/atom vs. decomposition to binary oxides for ferromagnetic (antiferromagnetic) configurations, respectively. The addition of Mg and Al has resulted in partial stabilization of the ferromagnetic state and destabilization of the antiferromagnetic state. The magnitude of the energies above the convex hull of synthetic valleyite and non-Ti containing natural valleyite ($x = 0$) suggests that these materials are energetically metastable at low (room) temperature.

The replacement of Al in $Ca_{3.5}Mg_{0.5}(Fe_4Al_2)O_{13}$ with Ti to form $Ca_{3.5}Mg_{0.5}(Fe_4Al_{1.875}Ti_{0.125})O_{13}$ (x= 0.125), the composition close to the experimentally derived composition of natural valleyite, $(Ca_{3.61}Mg_{0.39})(Fe_{3.97}Al_{1.91}Ti_{0.09})O_{13}$, results in a marked stabilization of the material compared to when no Ti is present. Both the ferromagnetic and antiferromagnetic arrangements result in these materials residing on the convex hull (note that the ferromagnetic arrangement is 30 meV/atom above the hull when considering its stability together with the antiferromagnetic arrangement), and have negative formation energies (i.e., are stable) relative to decomposition to the constituent binary oxides. At this time, it is unclear what role Ti plays in the stabilization of valleyite, however it is apparent that higher Ti concentrations than $x = 0.125$ (e.g. $x = 0.5$ to make $Ca_{3.5}Mg_{0.5}(Fe_4Al_{1.5}Ti_{0.5})O_{13}$) result in destabilization with an energy above the convex hull of 170 meV/atom (see Table 1). We note here the addition of Ti results in the reduction of Fe^{3+} to Fe^{2+}, as evidenced by the loss of 1 μ_B on Fe per Ti^{4+} added. From this result, we speculate there may be a range of Ti concentrations resulting in stabilization of the naturally occurring valleyite mineral, and that destabilization at higher Ti content may be due to Ti-Ti interactions and/or the instability of Fe^{2+} in the tetrahedral Fe-O bonding environment of the sodalite structure.

Comparisons can be made between the DFT-predicted magnetic moments and the measured magnetization of natural valleyite $(Ca_{3.61}Mg_{0.39})(Fe_{3.97}Al_{1.91}Ti_{0.09})O_{13}$. Simulating the ferromagnetic state of $Ca_4Fe_6O_{13}$ and $Ca_{3.5}Mg_{0.5}(Fe_4Al_2)O_{13}$ indicates that Fe^{3+} exists in the high spin state with a moment of 4.3 μ_B/Fe, with O carrying a small magnetic moment of about 0.25 μ_B/O. Note that ascribing the total magnetic moment to Fe results in an Fe moment of 5 μ_B/Fe, which is typical for Fe in the high spin state. For $Ca_{3.5}Mg_{0.5}(Fe_4Al_2)O_{13}$, these combined moments amount to a magnetization of ~20 μ_B/(formula unit) ≈7.6 emu/g. This value is in reasonable agreement with the experimentally measured valleyite magnetization value of ≈9.2 emu/g. We note here the stability calculations indicated that the ferromagnetic state tended to be slightly less stable than the antiferromagnetic state. However, it is worth noting that no effort was made to model ferrimagnetic or paramagnetic states of valleyite, so we cannot make quantitative comparisons of the relative stabilities of these magnetic states.

IMPLICATIONS

This study demonstrates that a combination of advanced synchrotron XRD (Xu et al. 2000, 2002, 2010; Zhang et al. 2002) with high-resolution TEM is a powerful approach to identify nano-minerals in geological systems and to determine their nanocrystalline structures (Xu et al. 2017b). Especially, the high brilliance and high coherence of synchrotron X-rays enables the clear separation of weak and broad XRD peaks of nanocrystalline phases, which cannot be resolved or detected by conventional XRD, particularly for complex, multiphase natural samples. In addition, direct imaging and analysis by high-resolution TEM combined with SAED and X-ray EDS spectra allow determination of the structures and chemistry of minerals at the nanoscale. We expect that this integrated approach will be employed to discover many new nano-minerals in the future.

Valleyite is a new magnetic material with low density framework structure. The magnetic exchange coupling in nano-minerals may hold the key for understanding the unusual magnetization phenomena seen in some igneous rocks from Earth, Mars and the moon (Heaman, 1997; Acuña et al. 1999; Stevenson, 2001). The observed exchange-coupled magnetic property between valleyite (soft magnet) and luogufengite (hard magnet) in the scoria samples will shed light on the paleo-magnetism, i.e., high remnant magnetization, of basaltic and related rocks. Furthermore, the magnetic valleyite phase with a sodalite-type structure may potentially be a functional magnetic material with magnetic, medical, and biochemical applications (Newsam, 1986).

ACKNOWLEDGMENTS

This work was supported by the NASA Astrobiology Institute (NNA13AA94A). Use of the Advanced Photon Source at Argonne National Laboratory was supported by the U. S. Department of Energy, Office of Science, Office of Basic Energy Sciences, under Contract No. DE-AC02-06CH11357. Los Alamos National Laboratory is operated by Los Alamos National Security LLC, under DOE Contract DE-AC52-06NA25396. The authors gratefully acknowledge use of facilities and instrumentation supported by NSF through the University of Wisconsin Materials Research Science and Engineering Center (DMR-1720415).

REFERENCES

Acuña, M.H., Connerney, J.E., Ness, N.F., Lin, R.P., Mitchell, D., Carlson, C.W., McFadden, J., Anderson, K.A., Reme, H., Mazelle, C., Vignes, D., Wasilewski, P., and Cloutier, P. (1999) Global distribution of crustal magnetization discovered by the Mars Global Surveyor MAG/ER experiment, Science, 284, 790-793.

Anisimov, V. I., Aryasetiawan, F., Lichtenstein, A. I. (1997) First-Principles Calculations of the Electronic Structure and Spectra of Strongly Correlated Systems: The LDA+U Method. Journal of Physics Condensed Matter. 9, 767–808.

Hackett, W.R., and Morgan, L.A. (1988*)* Explosive basaltic and rhyolitic volcanism of the eastern Snake River Plain. In: Link, P.K., and Hackett, W.R., eds., Guidebook to the Geology of Central and Southern Idaho: Idaho Geological Survey Bulletin 27, 283-301.

Hassan, I., Antao S. M., and Parise, J. B. (2004) Sodalite: High-temperature structures obtained from synchrotron radiation and Rietveld refinement. American Mineralogist 89, 359-364.

Heaman, L. M. (1997). Global mafic magmatism at 2.45 Ga: Remnants of an ancient large igneous province?. Geology, 25(4), 299-302.

Hughes, S.S., Smith, R.P., Hackett, W.R., and Anderson, S.R. (1999) Mafic Volcanism and Environmental Geology of the Eastern Snake River Plain, Idaho. In: Hughes, S.S., and Thackray, G.D., eds., Guidebook to the Geology of Eastern Idaho: Idaho Museum of Natural History, 143-168.

Jacobs, R., Booske, J., Morgan, D. (2012) Intrinsic defects and conduction characteristics of Sc_2O_3 in thermionic cathode systems. Physical Review B. 86(5), 054106.

Jacobs, R., Mayeshiba, T., Booske, J., Morgan, D. (2018) Material Discovery and Design Principles for Stable, High Activity Perovskite Cathodes for Solid Oxide Fuel Cells. Advanced Energy Materials 8(11), 1702708.

Jain, A., Ong, S. P., Hautier, G., Chen, W., Richards, W. D., Dacek, S., Cholia, S., Gunter, D., Skinner, D., Ceder, G., Persson, K. A. (2013) Commentary: The Materials Project: A Materials Genome Approach to Accelerating Materials Innovation. APL Materials, 1(1), 0111002.

Kneller, E.F., and Hawig, R. (1991)The exchange-spring magnet: a new material principle for permanent magnets. IEEE Transactions on Magnetics, 27(4), 3588-3560.

Kresse, G., and Furthmüller, J. (1996) Efficient Iterative Schemes for Ab Initio Total-Energy Calculations Using a Plane-Wave Basis Set. Physical Review B, 54(16), 11169–11186.

Kresse, G., and Joubert, D. (1999) From Ultrasoft Pseudopotentials to the Projector Augmented-Wave Method. Physical Review B, 59(3), 1758–1775.

Lee, S., and Xu, H. (2016). Size-dependent phase map and phase transformation kinetics for nanometric iron (III) oxides (γ→ ε→ α pathway). The Journal of Physical Chemistry C, 120(24), 13316-13322.

Lee, S., and Xu, H. (2018). The Role of ε-Fe_2O_3 Nano-Mineral and Domains in Enhancing Magnetic Coercivity: Implications for the Natural Remanent Magnetization. Minerals, 8(3), 97.

López-Sánchez, J., Muñoz-Noval, A., Serrano, A., Abuín, M., de la Figuera, J., Marco, J. F., Carmona, P. N., and de la Fuente, O. R. (2016). Growth, structure and magnetism of ε-Fe_2O_3 in nanoparticle form. RSC Advances, 6(52), 46380-46387.

Monkhorst, H., and Pack, J. (1976) Special Points for Brillouin Zone Integrations. Physical Review B, 13(12), 5188–5192.

Muxworthy, A.R., and Williams, W. (2006) Critical single-domain/multidomain grain sizes in noninteracting and interacting elongated magnetite particles: Implications for magnetosomes. Journal of Geophysical Research, 111, B12S12.

Namai, A., Sakurai, S., Nakajima, M., Suemoto, T., Matsumoto, K., Goto, M., Sasaki, S., and Ohkoshi, S.-I. (2009) Synthesis of an electronmagnetic wave absorber for high-speed wireless communication. Journal of American Chemical Society, 131, 1170-1173.

Neupane, D., Ghimire, M., Adhikari, H., Lisfi, A., and Mishra, S. R. (2017). Synthesis and magnetic study of magnetically hard-soft $SrFe_{12-y}Al_yO_{19}$-xWt.%$Ni_{0.5}Zn_{0.5}Fe_2O_4$ nanocomposites. AIP Advances, 7(5), 055602.

Newsam, J. M. (1986). The zeolite cage structure. Science, 231(4742), 1093-1099.

Ohkoshi, S. I., Sakurai, S., Jin, J., and Hashimoto, K. (2005). The addition effects of alkaline earth ions in the chemical synthesis of ε-Fe_2O_3 nanocrystals that exhibit a huge coercive field. Journal of Applied Physics, 97(10), 10K312.

Ong, S. P., Richards, W. D., Jain, A., Hautier, G., Kocher, M., Cholia, S., Gunter, D., Chevrier, V. L., Persson, K. A., Ceder, G. (2013) Python Materials Genomics (pymatgen): A robust, open-source python library for materials analysis. Computational Materials Science, 68, 314-319.

Perdew, J., Burke, K., Ernzerhof, M. (1996) Generalized Gradient Approximation Made Simple. Physical Review Letters, 77 (18), 3865–3868.

Peters, L., Knorr, K., Evans, J. S. O., Senyshyn, A., Rahmoun, N.-S., and Depmeier W. (2007) Proton positions in and thermal behaviour of the phase 4 $CaO \cdot Al_2O_3 \cdot 3\ H_2O$ and its thermal decomposition to |$(OCa_4)_2$|$[Al_{12}O_{24}]$-SOD, determined by neutron/X-ray powder diffraction and IR spectroscopic investigations. Zeitschrift für Kristallographie, 222, 365–375.

Russell, W.J., and Brisbin, W.C. (1990) Primary Fractures within a Tuff Cone, North Menan Butte, Idaho, USA. Journal of Volcanology and Geothermal Research, 40, 11-22.

Stevenson, D. J. (2001). Mars' core and magnetism. Nature, 412(6843), 214.

Torkian,T., and A. Ghasemi,A. (2018) Energy Product Enhancement in Sufficiently Exchange-Coupled Nanocomposite Ferrites, Journal of Magnetism and Magnetic Material, 469, 119-127.

Tucek, J., Zboril, R., Namai, A., and Ohkoshi, S. I. (2010). ε-Fe2O3: An advanced nanomaterial exhibiting giant coercive field, millimeter-wave ferromagnetic resonance, and magnetoelectric coupling. Chemistry of Materials, 22(24), 6483-6505.

Wang, Y., Han, T., Ding, Y. S., Zheng, Z., and Zheng, Y. Z. (2016). Sodalite-like rare-earth carbonates: a study of structural transformation and diluted magnetism. Dalton Transactions, 45(3), 1103-1110.

Xu, H., Lee, S., and Xu, H. (2017a) Luogufengite: A new nano-mineral of Fe_2O_3 polymorph with giant coercive field. American Mineralogist, 102(4), 711-719.

Xu, H., Lee, S., Xu, H., Jacobs, R., and Morgan, D. (2017b) Valleyite, IMA 2017-026. CNMNC Newsletter No. 38, August 2017, page 1035; Mineralogical Magazine, 81, 1033–1038.

Xu, H., Heaney, P.J., and Beall, G.H. (2000) Phase transitions induced by solid solution in stuffed derivatives of quartz: A powder synchrotron XRD study of the $LiAlSiO_4$-SiO_2 join. American Mineralogist, 85(7-8), 971-979.

Xu, H., Navrotsky, A., Balmer, M.L., and Su, Y. (2002) Crystal chemistry and phase transitions in substituted pollucites along the $CsAlSi_2O_6$-$CsTiSi_2O_{6.5}$ join: A powder synchrotron X-ray diffractometry study. Journal of the American Ceramic Society, 85(5), 1235-1242.

Xu, H., Zhao, Y., Zhang, J., Wang, Y., Hickmott, D.D., Daemen, L.L., Hartl, M.A., and Wang, L. (2010) Anisotropic elasticity of jarosite: A high-P synchrotron XRD study. American Mineralogist, 95(1), 19-23.

Ye, W., Chen, C., Wang, Z., Chu, I. H., and Ong, S. P. (2018) Deep neural networks for accurate predictions of crystal stability. Nature Communications, 9, 3800.

Zhang, J., Celestian, A., Parise, J.B., Xu, H., and Heaney, P.J. (2002) A new polymorph of eucryptite ($LiAlSiO_4$), ε-eucryptite, and thermal expansion of α- and ε-eucryptite at high pressure. American Mineralogist, 87(4), 566-571.

FIGURE CAPTIONS

Figure 1. Experimental and calculated XRD patterns (overlapping black and red lines, respectively) of a Fe-oxide sample dominated by luogufengite (L), valleyite (V), and hematite (H). The residual between the measured and calculated profiles is shown right under the XRD pattern. The weight percentages of mineral phases in the sample were calculated using the Rietveld method. The strongest peak (d_{112} = 3.628 Å) and the second strongest peak (d_{011} = 6.287Å) (see the insert at upper-left corner for the enlarged peaks) are very similar to the (102) diffraction peak from hematite and (110) diffraction peak from labradorite (~6.263 Å). The (011) peak from valleyite is also close to the (011) broad peak from luogufengite. Careful sample preparation and high-resolution synchrotron XRD greatly helped the discovery of valleyite. Broad peaks from luogufengite are due to its much smaller (nano-size) crystals (Xu et al. 2017b).

Figure 2. (a) Bright-field TEM image showing a valleyite crystal, together with much smaller crystals of luogufengite (Luo) and silica-dominated glass. The crystal displays forms of {100} and {111}. (b) A [001] zone-axis selected-area electron diffraction (SAED) pattern of valleyite. (c) Bright-field TEM image showing a valleyite crystal along the $[\bar{1}11]$-direction with its SAED pattern (d). An ideal crystal shape projected along the [111] direction is inserted at the lower-right corner. In (a) and (c), all the Miller indices show traces of planes perpendicular to the images. The (111) plane displays similarly as (110). Rounded corners are due to resorption at high temperature after the crystals formed.

Figure 3. (a) Bright-field TEM image showing a broken piece of valleyite crystal. (b) High-resolution TEM image and its FFT pattern (inserted at the lower-left corner) of valleyite from a

thin corner of the crystal. (c, d) SAED patterns of the valleyite crystal along the [001] and [12] zone-axes, respectively. All the SAED patterns indicate a body-centered Bravais lattice (*I*), i.e., $h + k + l = 2n$. **(e)** A representative X-ray EDS spectrum from valleyite. Cu peaks are from the holey carbon-coated Cu grid that holds the specimen. Si peak is from silica-rich glass coating and fluorescence from the Li-drifted silicon detector of the X-ray EDS system.

Figure 4. Polyhedral atomic models of the valleyite structure: (a) projection along the a-axis; and (b) projection along the [111] zone-axis. Brown tetrahedra: $(Fe,Al)O_4$; Large green sphere: Ca; Small red sphere: O.

Figure 5. Crystal structures of sodalite (Hassan et al. 2004), synthetic $Ca_4Al_6O_{13}$ (Peters et al., 2007) and the newly discovered valleyite. The unit cell of valleyite is slightly larger than that of synthetic $Ca_4Al_6O_{13}$. The framework changes through distortion of di-trigonal rings to accommodate the different sizes of $(Fe,Al)O_4$ tetrahedra or (Fe,Al)-O bond distances. For clarity, Na and Ca atoms are omitted.

Figure 6. Temperature dependence magnetization of the valleyite-bearing sample from 300 to 1000 K measured on warming in 1kOe.

Figure 7. Room-temperature magnetic hysteresis loops of (a) synthetic Al-bearing ε-Fe_2O_3, (b) valleyite (schematic), and (c) natural sample composed of valleyite, luogufengite and hematite.

Table 1. Powder X-ray diffraction data (*d* in Å) for valleyite.

d_{obs}	I_{obs}	d_{clac}	I_{clac}	*hkl*
6.2871	**45.1**	**6.2826**	**43.1**	**0 1 1**
4.4395	6.4	4.4425	5.3	0 0 2
3.6284	**100.0**	**3.6273**	**100.0**	**1 1 2**
3.1395	7.9	3.1413	5.2	0 2 2
2.8011	**39.6**	**2.8097**	**36.5**	**0 1 3**
2.5644	**32.1**	**2.5649**	**29.4**	**2 2 2**
2.3750	**27.3**	**2.3746**	**31.5**	**1 2 3**
2.2188	4.5	2.2213	1.1	0 0 4
2.0976	8.7	2.0942	10.9	1 1 4
1.9877	6.5	1.9868	8.5	0 2 4
1.8192	5.9	1.8136	6.5	2 2 4
1.5604	10.4	1.5707	13.5	0 4 4

Table 2. Chemical composition of valleyite.

Analysis No.	1	2	3	4	5	Average
Fe_2O_3 (wt.%)	49.21	49.62	49.89	49.58	49.56	49.57
CaO	31.58	31.70	31.54	31.49	31.58	31.58
Al_2O_3	15.31	15.05	14.94	15.48	15.23	15.20
MgO	2.52	2.39	2.39	2.58	2.38	2.45
TiO_2	1.38	1.25	1.25	0.87	1.25	1.20
Fe	3.94	3.98	4.01	3.97	3.99	3.97
Ca	3.60	3.62	3.61	3.59	3.62	3.61
Al	1.92	1.89	1.88	1.94	1.92	1.91
Mg	0.40	0.38	0.39	0.41	0.38	0.39
Ti	0.11	0.10	0.08	0.07	0.10	0.09
Average chemical formula: $(Ca_{3.61}Mg_{0.39})(Fe_{3.97}Al_{1.91}Ti_{0.09})O_{13}$						
Notes: All calculations are based on 13 oxygen atoms.						

Table 3. Atomic parameters of valleyite.

Space group ($I\bar{4}3m$)

Atom	Occupancy	x	y	z	U_{iso} (Å^2)*
Ca	$Ca_{0.90}$ $Mg_{0.10}$	0.1543 (7)	0.1543 (7)	0.1543 (7)	0.012
Fe	$Fe_{0.66}$ $Al_{0.32}$ $Ti_{0.02}$	$1/4$	$1/2$	0	0.012
O1	$O_{1.00}$	0.3602 (5)	0.3602 (5)	0.9107 (6)	0.020
O2	$O_{1.00}$	0	0	0	0.039

Lattice parameters: a = 8.8852 (7) Å
*From Peters et al. (2007)

Table 4. Bond distances (Å) for valleyite and synthetic $Ca_4Al_6O_{13}$.

Valleyite $Ca_4(Fe,Al)_6O_{13}$		Synthetic $Ca_4Al_6O_{13}$	
Fe-O1	1.770 (5) x 4	Al-O1	1.737 (4) x 4
Ca-O1	2.285 (9) x 3	Ca-O1	2.311 (5) x 3
Ca-O2	2.375 (7) x 1	Ca-O2	2.374 (18) x 1

Table 5. Summary of valleyite stability assessment from DFT calculations. For the stability values, the first/second value corresponds to the stability of the simulated ferromagnetic/antiferromagnetic state, respectively. Note for *x*=0.5 the antiferromagnetic state was not simulated. A summary of decomposition products and phase fractions can be found in the calculation output files included as part of the supplementary materials.

Simulated Valleyite Composition	**Energy above convex hull (meV/atom) (FM/AFM)**	**Formation energy relative to binary oxides (meV/atom) (FM/AFM)**
$Ca_4Fe_6O_{13}$	105 / 42	70 / 7
$Ca_{3.5}Mg_{0.5}(Fe_4Al_{2-x}Ti_x)O_{13}$ ($x = 0$)	86[1] / 74[2]	41[1] / 29
$Ca_{3.5}Mg_{0.5}(Fe_4Al_{2-x}Ti_x)O_{13}$ ($x = 0.125$)	0[3] / 0	-290 / -320
$Ca_{3.5}Mg_{0.5}(Fe_4Al_{2-x}Ti_x)O_{13}$ ($x = 0.5$)	170[4] / n/a	121[4] / n/a

[1] The 86 meV/atom stability value is the average over four Mg and five Al configurations, which have a combined range from 85-90 meV/atom. The corresponding average formation energy of 41 meV/atom has a range of 39-42 meV/atom.

[2] The 74 meV/atom stability value is the average over four antiferromagnetic ordering arrangements, which have a range from 70-79 meV/atom.

[3] As both the FM and AFM state lie on the convex hull, if both phases are included in the analysis then the FM state is 30 meV/atom, not 0 meV/atom, above the convex hull.

[4] The 170 meV/atom stability value is the average over four Ti configurations, which have a range from 168-173 meV/atom. The corresponding average formation energy of 121 meV/atom has a range of 118-123 meV/atom.

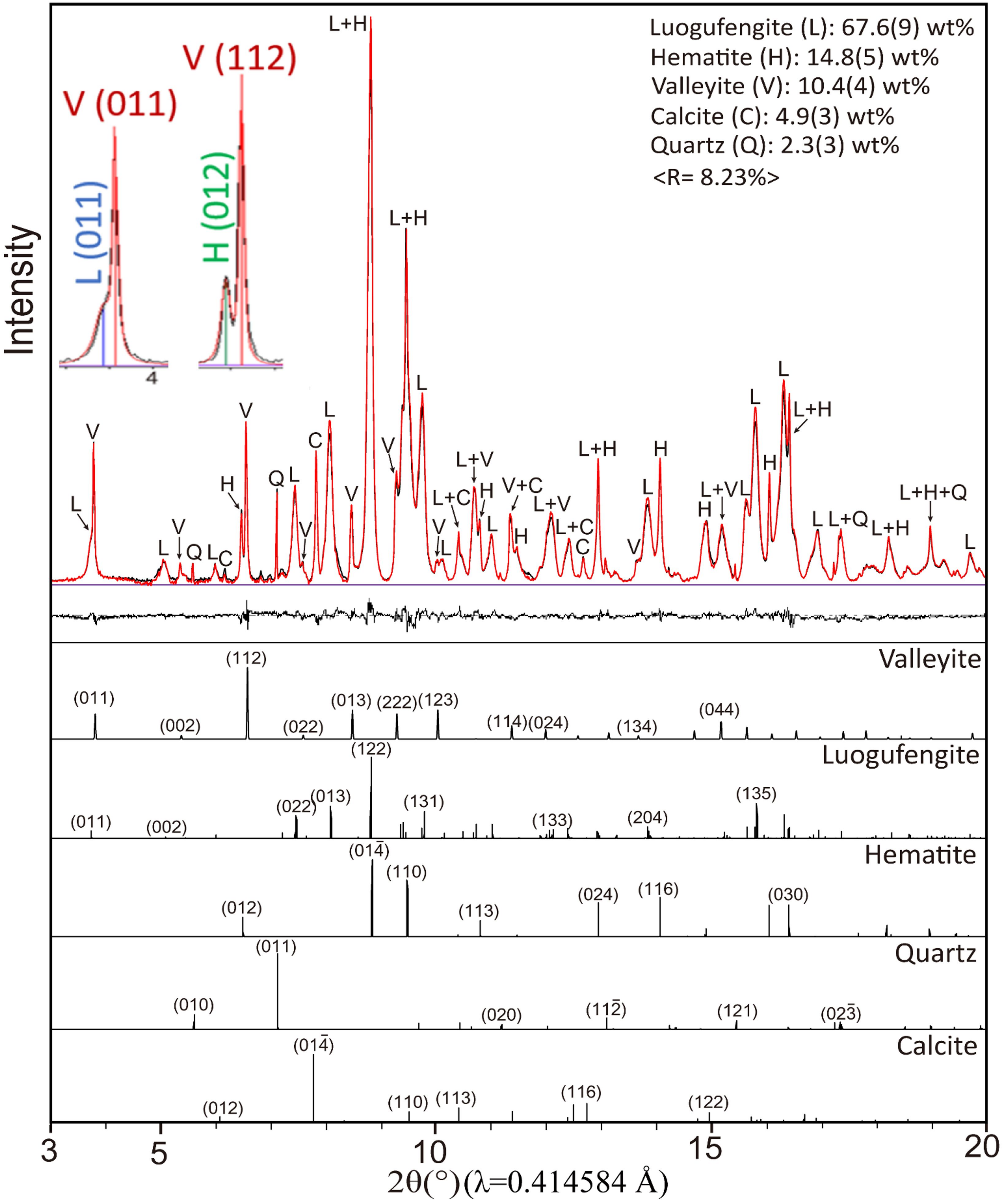
Luogufengite (L): 67.6(9) wt%
Hematite (H): 14.8(5) wt%
Valleyite (V): 10.4(4) wt%
Calcite (C): 4.9(3) wt%
Quartz (Q): 2.3(3) wt%
<R= 8.23%>
Intensity
V (011)
V (112)
L (011)
H (012)
4
L+H
L+H
L
V
L
C
L
V
L
V
H
V
Q
L
V
L
Q
L
C
L+C
L+V
H
L
V+C
L+V
L+C
L+H
H
L
V
L
H
L+VL
H
L
L
L+H
L
L+Q
L+H
L+H+Q
V
C
V
L
Valleyite
(011)
(002)
(112)
(022)
(013)
(222)
(123)
(114)
(024)
(134)
(044)
Luogufengite
(011)
(002)
(022)
(013)
(122)
(131)
(133)
(204)
(135)
Hematite
(012)
(01$\bar{4}$)
(110)
(113)
(024)
(116)
(030)
Quartz
(010)
(011)
(020)
(11$\bar{2}$)
(121)
(02$\bar{3}$)
Calcite
(012)
(01$\bar{4}$)
(110)
(113)
(116)
(122)
3
5
10
15
20
2θ(°)(λ=0.414584 Å)

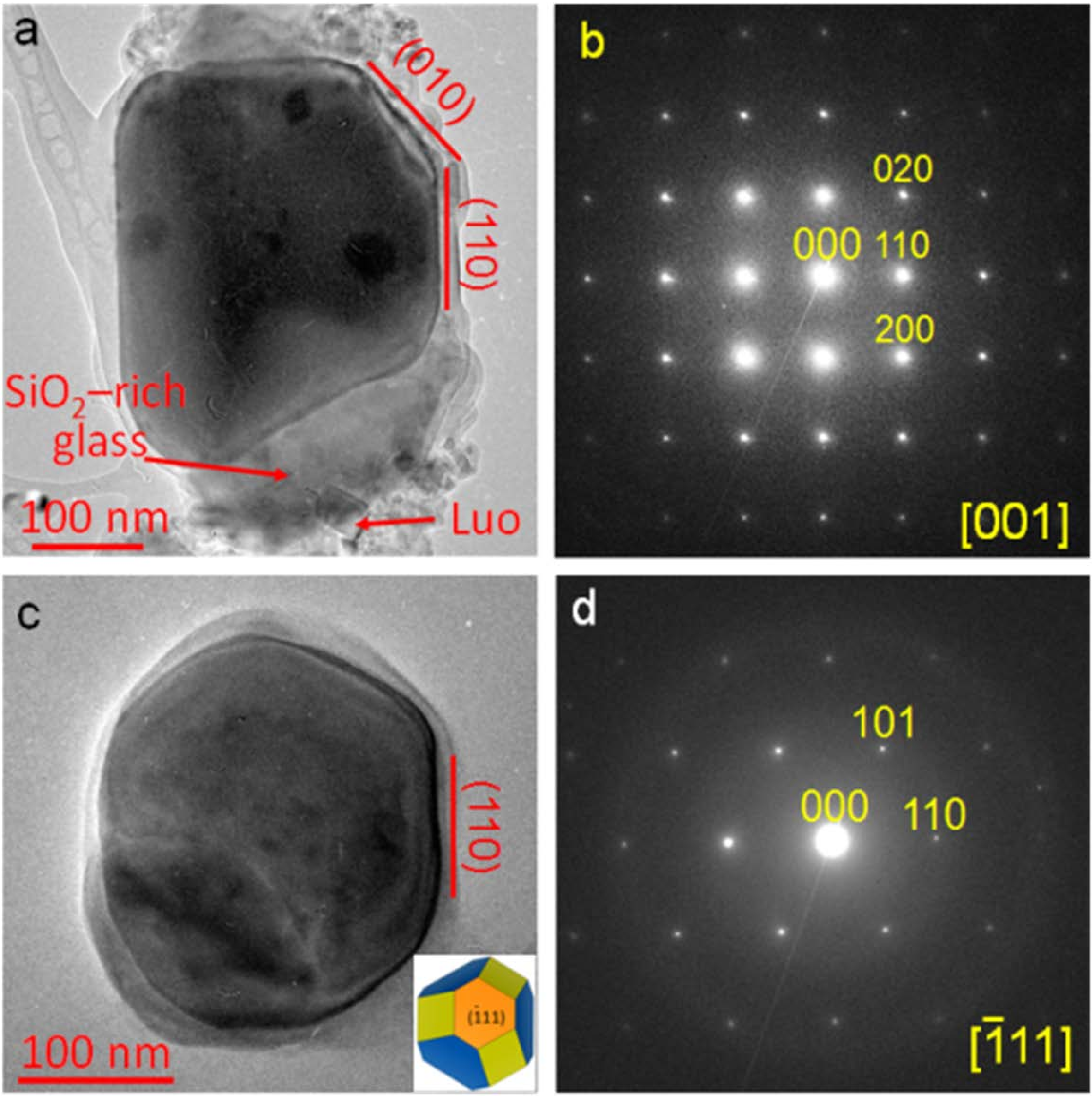
a
(010)
(110)
SiO$_2$–rich glass
100 nm
Luo
b
020
000
110
200
[001]
c
(110)
($\bar{1}$11)
100 nm
d
101
000
110
[$\bar{1}$11]

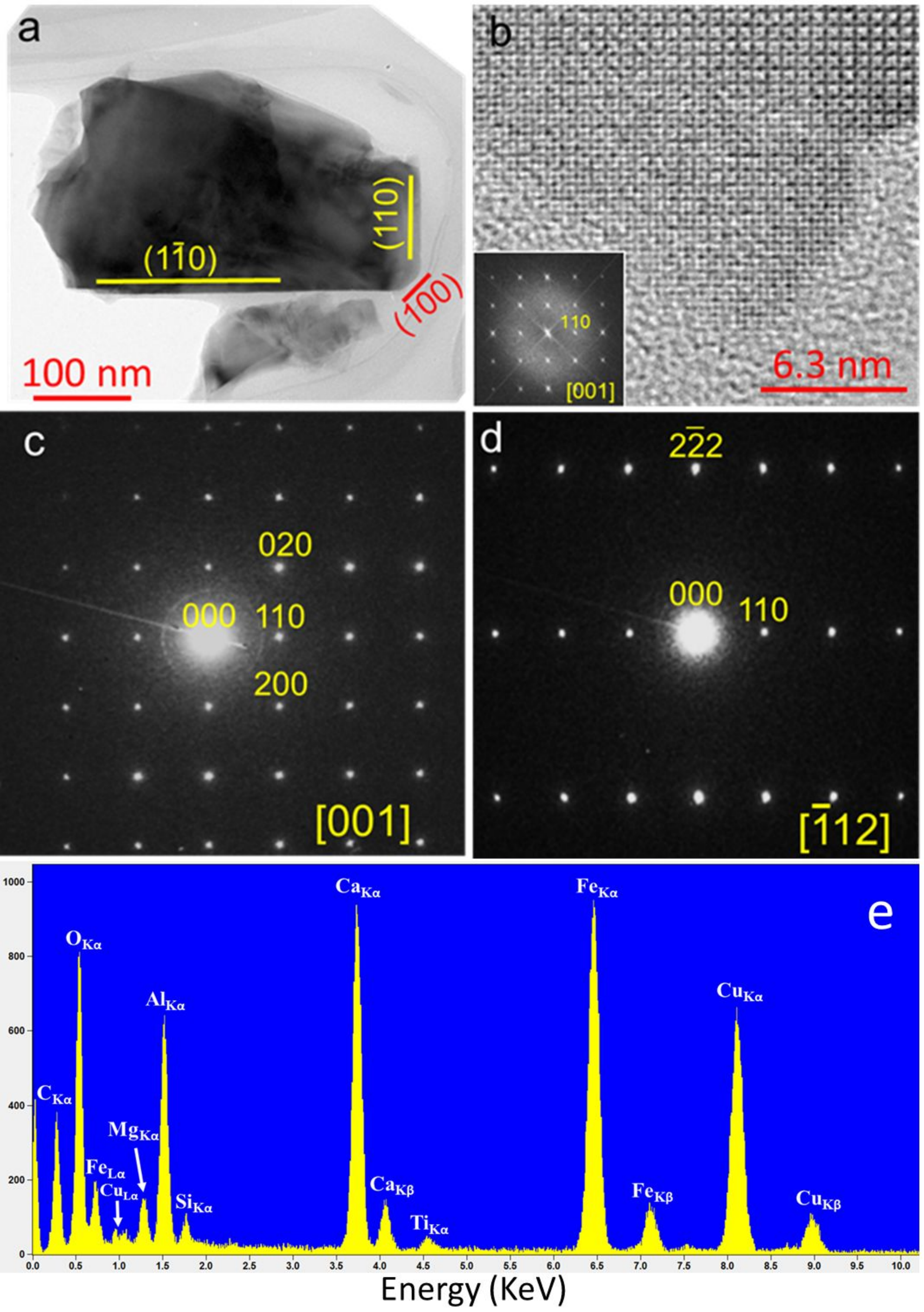
a
(1$\bar{1}$0)
(110)
($\bar{1}$00)
100 nm
b
110
[001]
6.3 nm
c
020
000
110
200
[001]
d
2$\bar{2}$2
000
110
[$\bar{1}$12]
e
C$_{K\alpha}$
O$_{K\alpha}$
Fe$_{L\alpha}$
Cu$_{L\alpha}$
Mg$_{K\alpha}$
Al$_{K\alpha}$
Si$_{K\alpha}$
Ca$_{K\alpha}$
Ca$_{K\beta}$
Ti$_{K\alpha}$
Fe$_{K\alpha}$
Fe$_{K\beta}$
Cu$_{K\alpha}$
Cu$_{K\beta}$
0
200
400
600
800
1000
0.0
0.5
1.0
1.5
2.0
2.5
3.0
3.5
4.0
4.5
5.0
5.5
6.0
6.5
7.0
7.5
8.0
8.5
9.0
9.5
10.0
Energy (KeV)

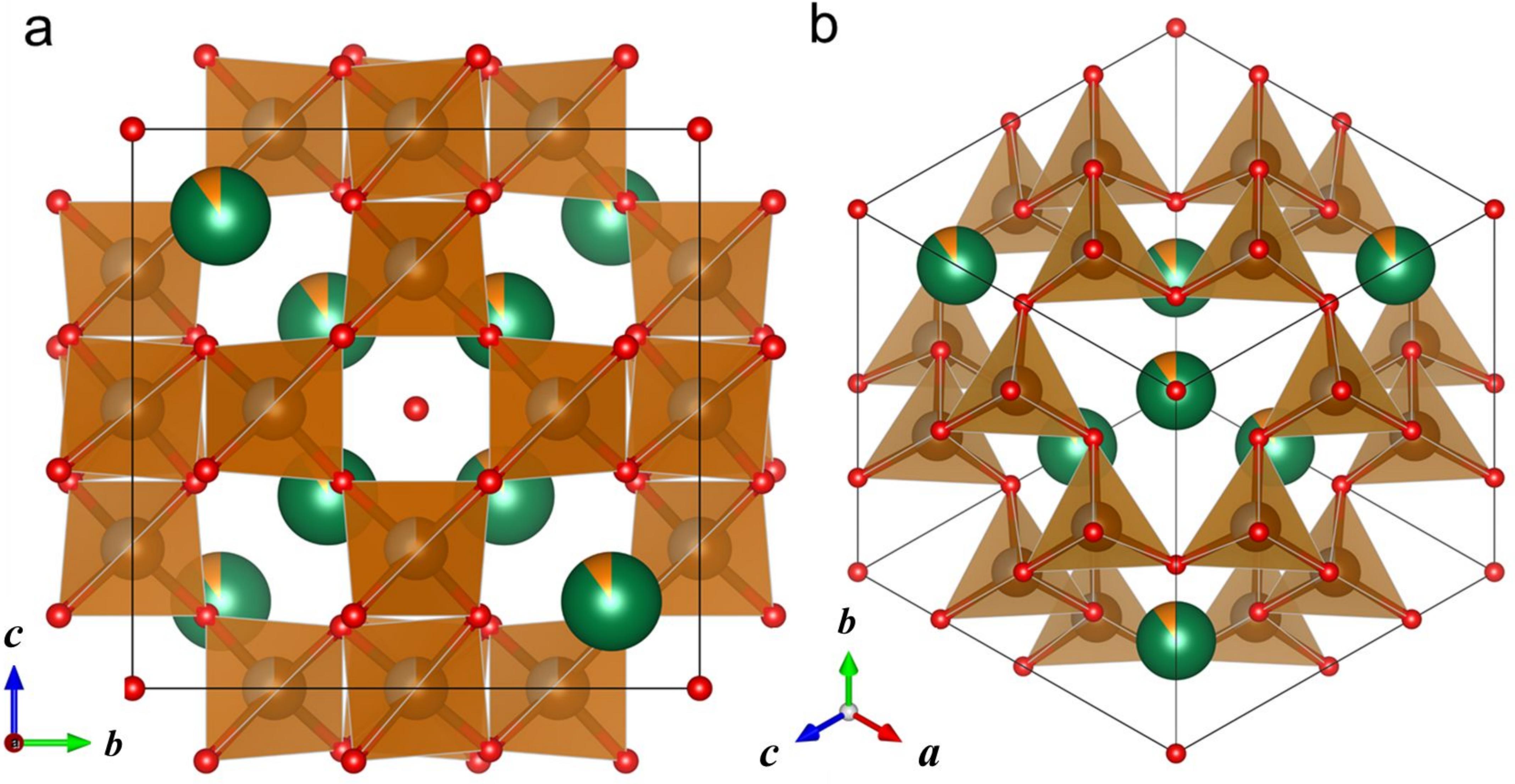
a
c
b
b
b
c
a

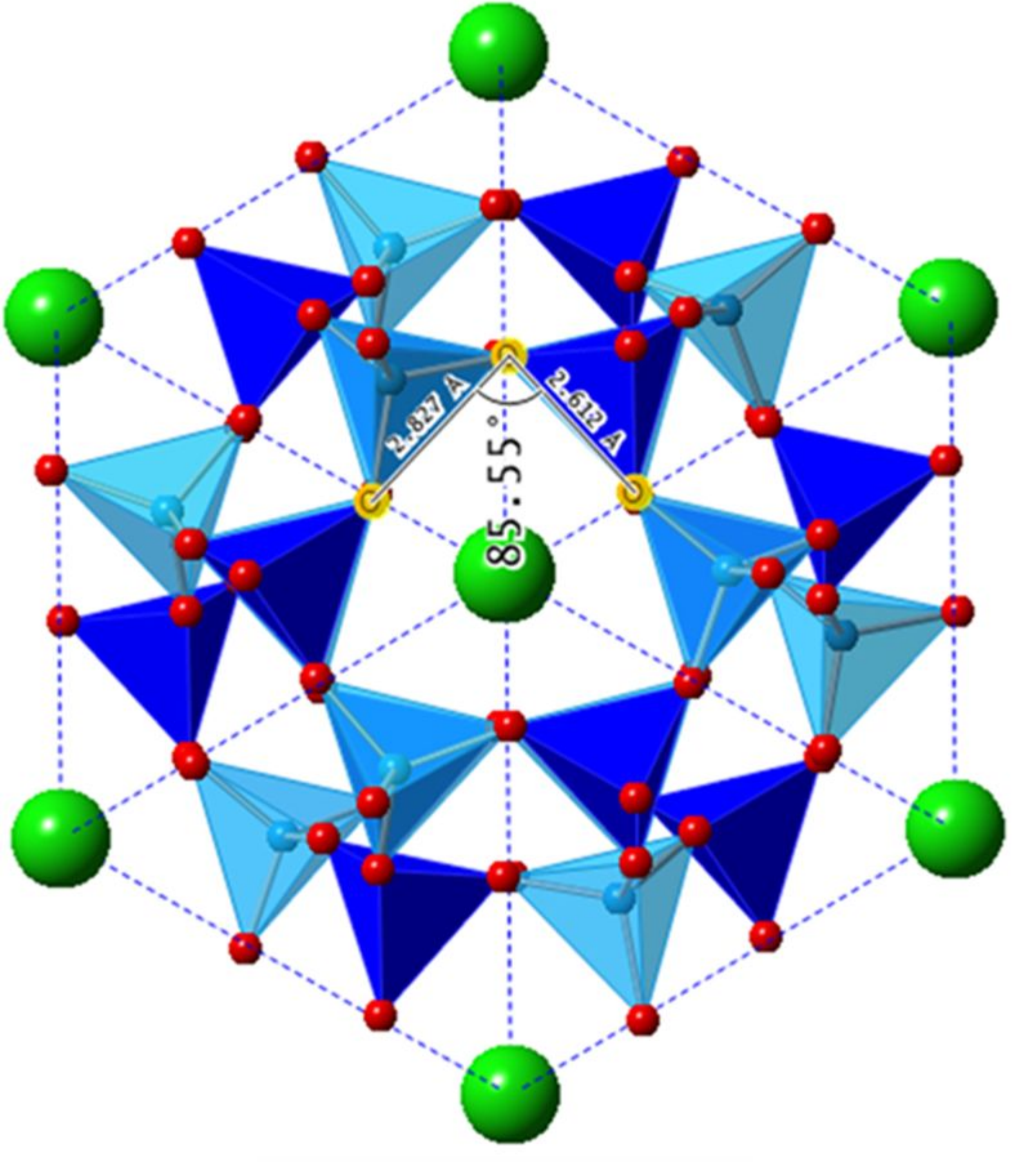

Sodalite

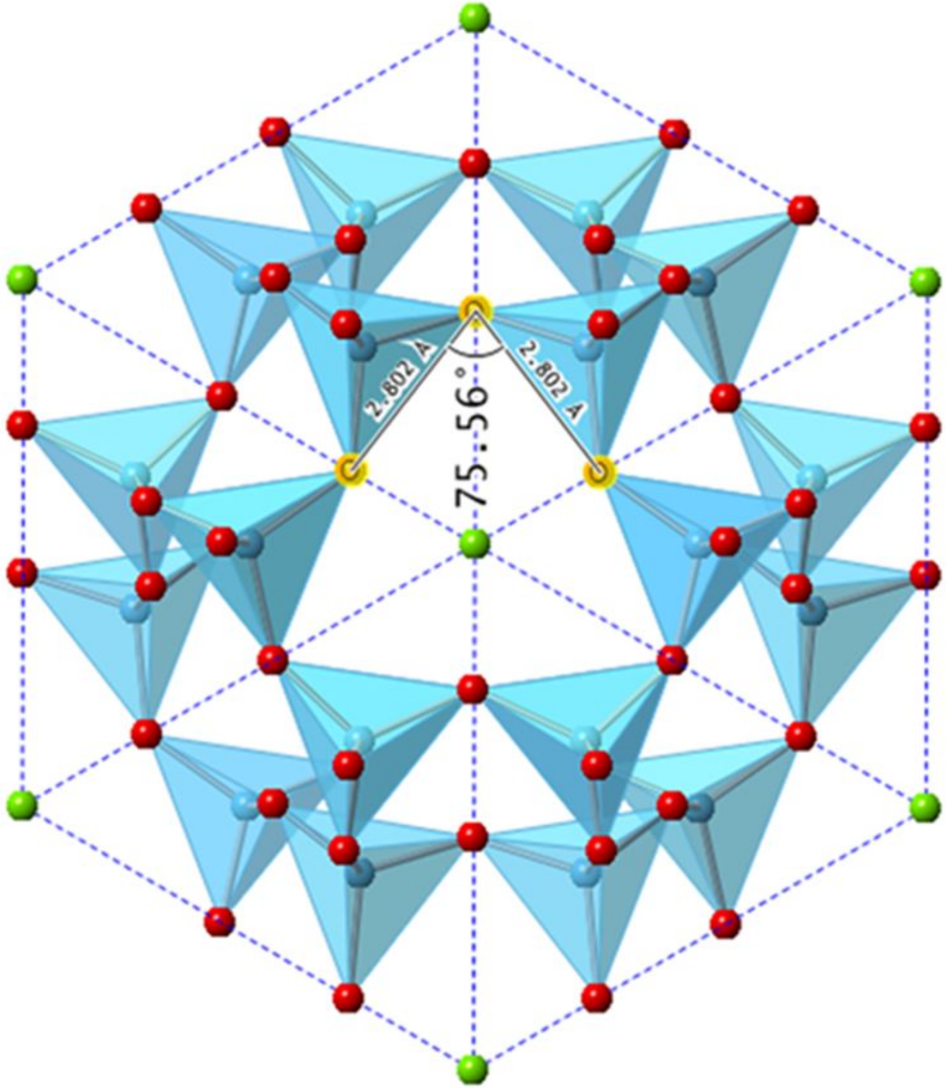

Synthetic $Ca_4Al_6O_{13}$

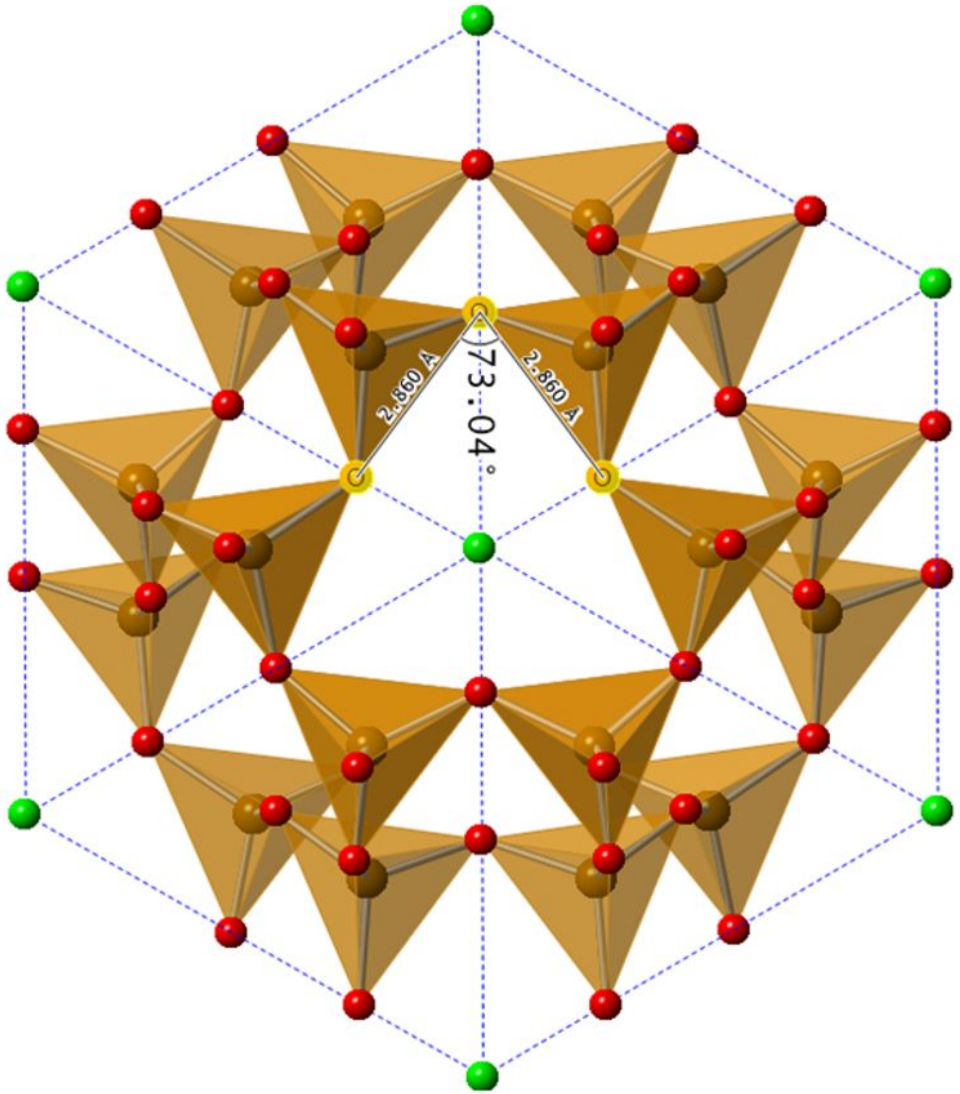

Valleyite

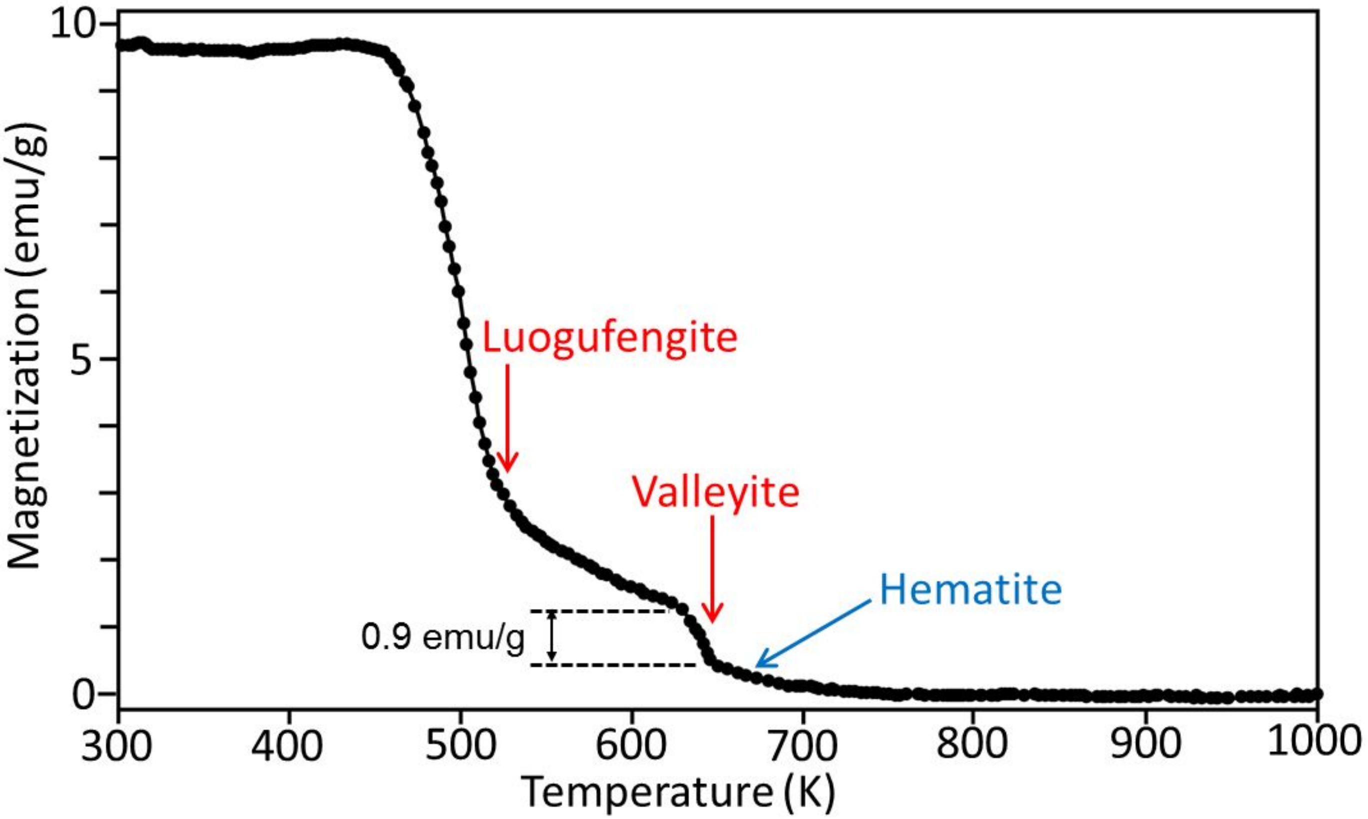
10
5
0
Magnetization (emu/g)
300
400
500
600
700
800
900
1000
Temperature (K)
Luogufengite
Valleyite
Hematite
0.9 emu/g

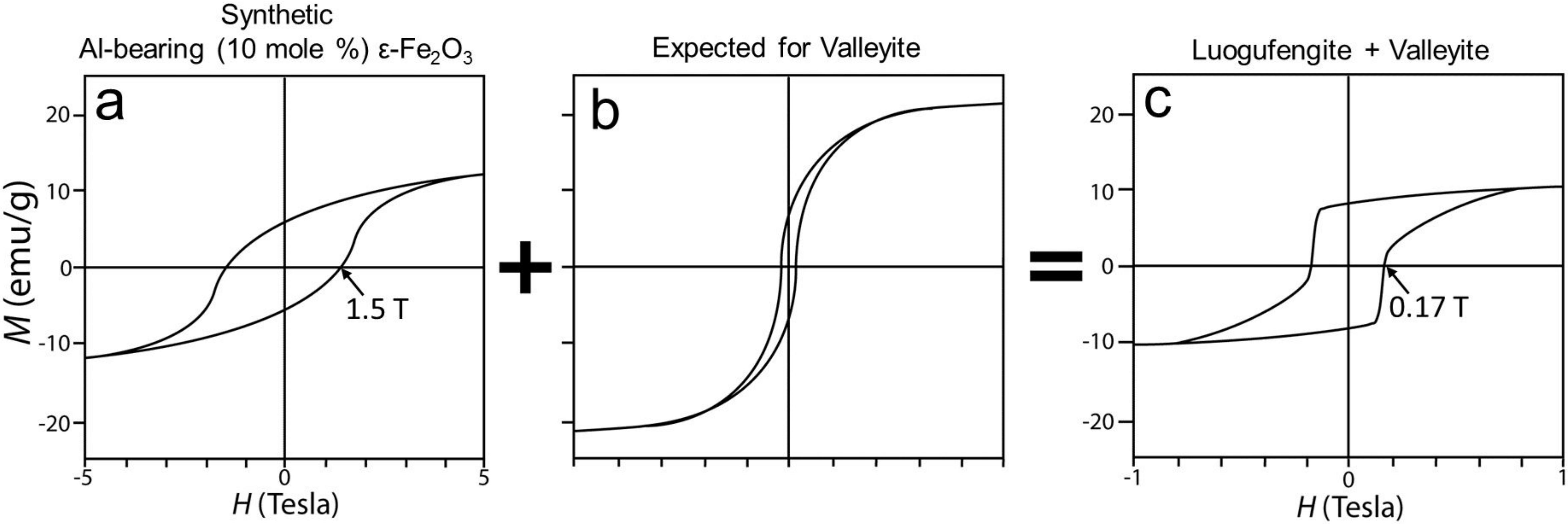
Synthetic
Al-bearing (10 mole %) ε-Fe$_2$O$_3$
a
1.5 T
M (emu/g)
20
10
0
-10
-20
-5
0
5
H (Tesla)
+
Expected for Valleyite
b
=
Luogufengite + Valleyite
c
0.17 T
20
10
0
-10
-20
-1
0
1
H (Tesla)